Solar thermochemical fuel production from H2O and CO2 splitting via two-step redox cycling of reticulated porous ceria structures integrated in a monolithic cavity-type reactor

Anita Haeussler, Stéphane Abanades, Anne Julbe, Julien Jouannaux, Bruno Cartoixa

Solar thermochemical fuel production from H_2O and CO_2 splitting via two-step redox cycling of reticulated porous ceria structures integrated in a monolithic cavity-type reactor

Anita HAEUSSLER[1], Stéphane ABANADES[1*], Anne JULBE[2], Julien JOUANNAUX[2], Bruno CARTOIXA[3]

[1] Processes, Materials and Solar Energy Laboratory, CNRS-PROMES, 7 Rue du Four Solaire, 66120 Font-Romeu, France

[2] Institut Européen des Membranes, IEM, UMR-5635, ENSCM, CNRS, Univ Montpellier, Place Eugène Bataillon, 34095 Montpellier cedex 5, France

[3] ALSYS-CTI, 382 avenue du Moulinas, 30340 Salindres, France

[*] Corresponding author: Tel +33 (0)4 68 30 77 30

E-mail address: stephane.abanades@promes.cnrs.fr

Abstract.

Solar thermochemical H_2O and CO_2 splitting cycles represent an efficient route for converting high temperature concentrated solar heat into valuable chemical energy carriers (solar fuels). A new monolithic solar reactor compatible with ceria redox reactions was designed, constructed and tested under concentrated solar radiation. The ceria redox material was shaped and integrated as reticulated porous structures with controlled cell sizes and gradient (10-60 ppi, pores per inch) enabling efficient volumetric solar radiation absorption and micro-scale interconnected porosity favouring the solid-gas reactions. Temperature-swing redox cycling experiments were performed to demonstrate solar reactor reliability during continuous operation. The foams were first thermally activated by increasing the reactor temperature (1400-1450°C) for O_2 release and then exposed to H_2O or CO_2 stream to produce pure H_2 or CO (700-1100°C), allowing cyclic operation in the same reactor. The influence of operating conditions (including reduction and oxidation temperatures, pressure and type of oxidizing gas) on reactor performance was investigated. An increase of the reduction temperature or a decrease of the operating pressure improved both the ceria reduction extent and fuel production yields (up to 341 µmol/g), while a decrease of the CO:CO_2 ratio (by increasing total inlet gas flow-rate) or an increase of the inlet CO_2 concentration enhanced oxidation

rates (up to 9.3 mL/g/min). The obtained fuel production rates outperformed the maximum previously reported values by up to 8 times using the highly-reactive manufactured ceria porous foams cycled between 1400°C and 900°C with oxidation performed in 100% CO_2 upon dynamic cooling. An average H_2/CO production of ~280 Ncm^3/cycle (64 cycles performed) was achieved with solar-to-fuel efficiency up to ~7.5% and remarkable material performance stability.

Keywords: solar energy, CO_2 valorization, hydrogen, syngas, ceria redox cycle, open-cell foam, volumetric reactor

1. Introduction

The harnessing of the huge energy potential of solar radiation and its effective conversion to chemical energy carriers is a subject of primary technological interest [1]. This ambitious goal provides a CO_2-free and cost-effective pathway to fuel the vehicles and economies of the future. H_2 and other synthetic fuels are attractive long-term energy carriers if they are generated by the use of unlimited renewable energy without harmful emissions [2,3]. The ideal long-term raw materials for H_2 and CO production (both precursors to synthetic liquid fuels) are water and carbon dioxide:

$$xCO_2 + (x+1)H_2O + \text{Solar Energy} \rightarrow xCO + (x+1)H_2 + (x+0.5)O_2 \quad (1)$$

Using solar power to produce the highly-demanded reaction intermediate, syngas, directly from H_2O and captured CO_2, provides a promising path towards sustainable energy conversion into valuable solar fuels [4–6]. Such a solar process is relevant to upgrade low cost feedstocks with no calorific value (H_2O and CO_2) into high value solar fuels. The overall process that results in the net conversion of H_2O and CO_2 into carbon-neutral liquid fuels from solar energy is thus equivalent to a reverse combustion.

$$xCO_2 + (x+1)H_2O + \text{Solar Energy} \rightarrow C_xH_{2x+2}\ (\text{liquid fuel}) + (1.5x+0.5)O_2 \quad (2)$$

The unfeasibility of direct H_2O and CO_2 splitting (thermolysis) with current or near-future technology leads to the development of multi-step cycles with the same net effect, i.e. the dissociation of H_2O/CO_2 into constitutive compounds [7,8]. The advantages of this approach are numerous and varied. First, the temperature of the decomposition reaction in the cycle is

much lower than the required temperature for direct thermolysis. Second, such a multi-step process produces O_2 and H_2 (or CO) in separate steps, without the need to perform any high-temperature separation of the gas species, and there is no risk to form an explosive gas mixture.

The solar chemistry for two-step cycles involves reactions of metal oxide redox pairs. In a first step driven by solar thermal energy, reduction of the metal oxide generates an active oxygen-deficient material with pure oxygen release (which can also be valorized [4,5,9,10]) according to reaction (3). In a second step, oxidation of the active redox material (reduced state of the considered metal oxide) by H_2O and/or CO_2 produces H_2 and/or CO according to reaction (4) [11–14].

Thermal reduction (endothermic): $M_xO_y \rightarrow M_xO_{y-\delta} + \delta/2\ O_2$ (3)

H_2 and/or CO generation (exothermic): $M_xO_{y-\delta} + \delta\ H_2O/CO_2 \rightarrow M_xO_y + \delta\ H_2/CO$ (4)

Among the relevant potential redox materials, ceria (CeO_2) is attractive given the high oxygen exchange properties in the crystal lattice, rapid and reversible transition between Ce^{4+} and Ce^{3+} oxidation states, and stable cubic fluorite crystal structure during cycling [15–21]. Indeed, the crystalline structure of non-stoichiometric cerium oxides remains stable during solid-state reactions, while the lattice accommodates changes in anion or cation vacancies concentrations (e.g., $CeO_2(s) \rightarrow CeO_{2-\delta}(s)$). Doping or substitution strategies are often employed to adjust/improve their thermodynamic, kinetic and physical properties [22,23]. For example, doping ceria with Zr^{4+} is known to increase its oxygen storage capacity and to enhance Ce^{4+} to Ce^{3+} reduction due to its ability to destabilize the fluorite lattice [24–30] but the oxidation rate is strongly hindered. The novel ceria cycle was first proposed by PROMES-CNRS in 2006 [31] and since then, ceria-based materials have been investigated for solar thermochemical splitting of both H_2O and CO_2 [32–34]. Maximum fuel production rates reported to date were achieved in a solar reactor simulator using ceria foam with dual-scale porosities heated by artificial light, at a high reduction temperature of 1500°C and low pressure of 10 mbar, yielding CO production rate up to 1.2 mL min^{-1} g^{-1}_{CeO2} [35–37]. Attractive results have been obtained, although there is still room for improvement regarding the specific productivity of H_2 and CO per gram of material and per cycle, the fuel production rates and the material stability upon cycling. Improved material design and integration of active redox materials in solar reactors are two important requirements to promote further expansion of solar fuels production by this approach.

This study addresses the design, demonstration and qualification of a new solar reactor operating continuously based on porous monolithic structures, with enhanced efficiency and scalability for future applications. Heterogeneous reactions benefit from active materials with easily accessible pores and high surface areas to promote oxygen transport and exchange properties. The reactive ceria was thus shaped as porous structures with interconnected porous network (reticulated porous ceramics, RPC), capable to absorb concentrated solar radiation, able to be easily integrated in the solar receiver/reactor and offering long-term thermal stability. The final structure must exhibit high macro-scale porosity (for access of solar radiation) and should act as an efficient solar absorber. In addition, micro-scale interconnected porosity is beneficial for access of gaseous H_2O/CO_2 reactants and products release, thus favouring uniform reaction throughout the structure.

The monolithic configuration is advantageous compared to fluidized bed, aerosol flow, or particle-entrained flow reactors, because it does not impose constraints regarding the minimum gas flow rate required for reactor operation as the reactive structured material remains fixed inside the reactor (non-stoichiometric ceria remains solid throughout the redox process) [38]. Particle transport between reaction steps is therefore bypassed. Such a concept avoids the need for continuous powder feeding and collection from the reactor. As a consequence, solid flow in process is eliminated. The inert gas flow was only used as purge gas to transport the evolved gas species (O_2 and H_2/CO) to the reactor outlet. In particular, the inlet gas flow rate was not linked to the amount of involved reacting material and it could thus be tuned to assess the effect of Ar dilution or oxidant gas concentration (steam or CO_2). In addition to the concentration, the amount of oxidant gas (affecting the $CO:CO_2$ or $H_2:H_2O$ ratio) was also identified as a decisive factor influencing the reaction rate during CO or H_2 production from CO_2 or H_2O splitting.

In this study, a directly-irradiated monolithic solar reactor was designed and operated for thermochemical H_2O and CO_2 splitting via ceria redox cycling with temperature-swing between reaction steps. The ceria material was loaded inside the reactor cavity as a reactive cylindrical open-cell foam hollowed at its center to favour radiation entrance and uniform absorption. The experimental campaign was conducted using a parabolic solar concentrator at CNRS (Odeillo, France). The following sections describe the main reactor components and characteristics, and the results of parametric studies of the cyclical reactions.

2. Experimental set-up

2.1. Specifications of the solar reactor

The solar reactor consists of a cavity-type cylindrical absorber heated by concentrated solar energy (Fig. 1). It is based on the directly-irradiated concept and it is chiefly composed of a vertical tubular cavity (80 mm height, 50 mm inside diameter, 60 mm outside diameter) acting as a blackbody solar receiver. Alumina was selected as the high-temperature wall material because it is thermally resistant while it is chemically inert in both reducing and oxidizing conditions. Thus, chemical interactions between the reactant and the reactor wall are avoided. A transparent hemispherical Pyrex glass window is fixed at the front of the reactor to allow solar radiation entering within the cavity while separating the cavity chamber from the surrounding air atmosphere. With this arrangement, the irradiated reaction zone in which the cycling redox reactions occur is maintained under controlled atmosphere. The window hemispherical shape is selected to position the window away from the focal point, thus avoiding glass overheating, which is requested for stable and reliable reactor operation during repeated cycles at the high-temperature processing conditions. The cavity made of alumina is designed to absorb the concentrated solar power via the front aperture plate also made of alumina (18 mm-diameter aperture). The aperture is placed at the focal point of the solar concentrating system (0.85 m from the parabolic mirror) where the solar flux density can reach over 10 MW/m^2, thus representing 1.5 kW of maximum thermal power absorbed by the cavity (for a direct normal irradiation DNI of 1 kW/m^2). The cavity walls are well insulated by using a porous alumino-silicate fibrous layer directly wrapping the ceramic cavity in order to minimize thermal conductive losses (total thickness of 3.6 cm on each side, 14 cm of external diameter and 14.6 cm height). A board of zirconia felt (2 mm thickness) is also used to insulate the front alumina wall of the aperture plate, thereby reducing the radiative losses at the upper front.

The height of the foam inside the cavity was about 50 mm and it was hollowed at its center to promote radiative heat transfer and absorption along the annular foam height, thereby favouring uniform heating of the whole reacting ceria structure.

The injected gas flows in the downward direction from the top to the bottom of the cavity to favour temperature homogenization. Ar gas flow is continually injected in the window area to provide inert gas atmosphere; it then enters the cavity via the aperture and sweeps the inner

cavity volume. In addition, an auxiliary gas inlet (6 mm alumina tube) is positioned at the top of the cavity below the aperture for rapid gas composition switch between reduction and oxidation steps. Ar is injected during reduction step whereas a mixture of Ar and CO_2 (or steam) is injected during oxidation step. The gas then flows through the porous ceria structure inside the cavity and exits at the bottom via a single outlet port located at the center. The gas composition is controlled and adjusted via mass-flow controllers (MFC, Brooks Instruments model SLA5850S). Different MFCs were used to control the flowrates of purge gas (Ar, 99.999% purity, O_2 content below 2 ppm) and CO_2 (99.995% purity). Water was injected using a liquid mass flow controller (range 0-60 g/h, accuracy ±1% of full scale) via an alumina capillary settled inside the auxiliary tube inlet and heated by the nearby cavity. Water was thus vaporized inside the heated capillary and was then transported by the surrounding carrier gas to the cavity volume.

Different temperature sensors were used to control the reactor temperature at different locations and heights (at the external cavity wall and in contact with the reactive foam). The foam temperature was measured directly via three B-type (Pt–Rh) thermocouples (T1 at the bottom of the cylindrical part, i.e. 60 mm from the cavity top, T2 at the upper part, i.e. 40 mm from the cavity top, and T3 below the foam, i.e. 80 mm from the cavity top). Besides, an optical solar-blind pyrometer operating at 4.8-5.2 μm also monitored the temperature of the cavity by pointing in the central hollow foam via a CaF_2 porthole. The reactor pressure was measured by pressure transmitters placed at the gas inlets (window and auxiliary gas) and cavity. The reactor was operated at atmospheric pressure in the cavity (about 0.85 bar at the experimental site altitude, 1500 m) and the pressure drop due to the foam was negligible. In addition, low pressure experiments with flowing gas were also performed by continuously pumping at the reactor outlet (using a primary vacuum pump) in order to study the effect of pressure on the reduction extent and fuel production yield.

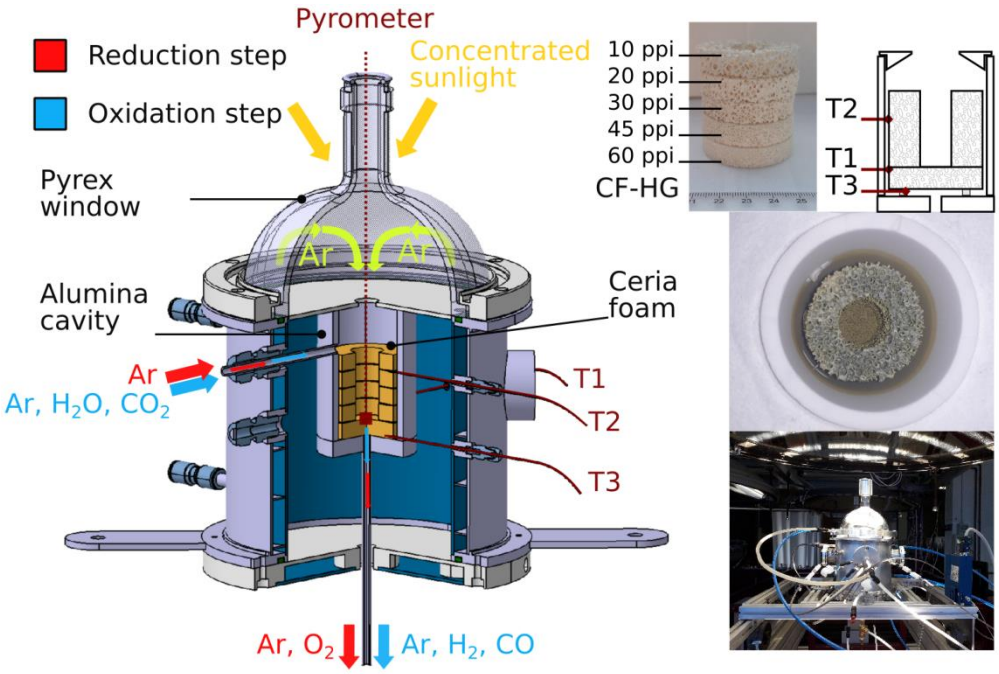

Figure 1: (left) Schematic illustration of the 1.5 kW_{th} monolithic solar reactor for ceria redox cycling to produce H_2 and CO, (right) top: photo of the foam with graded porosity and scheme of thermocouples position, middle: photo of the CF-MG foam inside the cavity after cycling, bottom: SUNFUEL solar reactor during on-sun testing.

2.2. Materials and methods

The experiments were carried out at the focus of a vertical-axis medium size solar furnace comprising a sun-tracking heliostat and a parabolic dish solar concentrator (2 m-diameter, Gaussian flux density distribution). The focal point of the concentrator (0.85 m ahead of the parabolic mirror) was located at the cavity aperture for maximum solar radiation absorption inside the cavity receiver. The absorbed solar power that determines the reactor temperature was controlled and adjusted by the means of an intermediate shutter placed between the heliostat and the solar concentrator (below the reactor), thus enabling heating/cooling rates and temperature control. The reduction and oxidation steps were performed alternately via temperature-swing cycling while switching the gas flow between each cycle step.

The reactor was first connected to a vacuum pump to remove remaining air, and then purged with Ar inert gas before further solar heating. Complete removal of residual oxygen before starting the reduction step was ascertained by the O_2 concentration below 10 ppm in the flowing gas. A trace O_2 analyzer with electrochemical cell (Systech, range from 0.1 ppm to 1%, precision ±2% of reading) was used to measure online the O_2 concentration in the outlet gas. After purging, the reactor was gradually heated with a stable heating rate up to the

maximal reduction temperature by stepwise shutter opening. During heating in Ar (Q_{Ar}=1.2 NL/min), O_2 was continuously released from ceria and its concentration increased steadily in response to the heating rate. The start of reduction was detected after a period of reactor heating when approaching ca. 900°C. The material reduction was continuously monitored by measuring the outlet O_2 concentration (used to calculate the O_2 production rate). Once reaching the temperature dwell, the O_2 concentration dropped smoothly because thermodynamic equilibrium was progressively reached when stabilizing the temperature. Then, the temperature was decreased by closing the shutter, which fastened the drop of O_2 concentration. The reduction step was completed when O_2 concentration dropped to values below 10 ppm. The oxidation step was subsequently conducted by injecting the reactive gas flow (water steam or CO_2) to produce H_2 or CO. The oxidant gas was injected under isothermal (i.e. once the targeted oxidation temperature was steady) or non-isothermal conditions (i.e. below a given temperature during free cooling with no solar energy input). CO (and CO_2) concentrations in the exhaust gas were measured on-line (concentration as a function of time profiles) by a specific analyzer with NDIR sensors (MGA3000, full scale: 0–30% for CO, 0-100% for CO_2, precision ±1% of full scale). H_2 was also analyzed continuously thanks to a specifically devoted H_2 analyzer based on thermal conductivity detection (catharometer for Ar/H_2 binary mixture, scale: 0-10%, precision: 1% of full scale), in order to quantify the H_2 produced during the reaction progress. H_2 or CO were detected few seconds after steam or CO_2 injection (< 10 s) and their concentration reached a maximum corresponding to the peak fuel production rate. After the peak, the concentration returned progressively to zero and the oxidizing gas injection was stopped to proceed to the next cycle by increasing the temperature again for the reduction step. Before gas analysis, the outlet gas flowed through a set including a bubbler to eliminate steam in excess and a gas drying unit (desiccant column) to protect the analytical instrument. In the case of H_2O splitting, the excess water was entirely condensed and trapped and the gas analyzed was thus composed of a binary mixture of Ar/H_2. In the case of CO_2 splitting, the outlet gas was composed of unreacted CO_2 in addition to Ar and CO. The whole process parameters (temperatures, pressures, gas flowrates, outlet gas concentrations) were recorded every seconds by an automated data acquisition system (Beckhoff).

The time-dependent gas production rates (F_i) were calculated from the inlet carrier gas flow rate (F_{Ar}) and the measured outlet gas mole fractions (y_i):

$$F_i=F_{Ar}.y_i/(1-y_i) \quad (5)$$

where i denotes O_2 or H_2.

In the case of CO_2 splitting, the outlet CO production rate was determined as:

$$F_{CO,outlet}=(F_{Ar}+F_{CO2,outlet}+F_{CO,outlet}).y_{CO} \quad (6)$$

where $$F_{CO,outlet}+F_{CO2,outlet}=F_{CO2,inlet} \quad (7)$$

The amounts of gas produced (O_2 and H_2 or CO) were then determined by time integration of the gas production rates over the duration of the reduction and oxidation steps ($\int F_i.dt$). The oxidant conversion defined as the molar ratio of oxidant decomposed to oxidant in the feed was also evaluated.

Energy efficiencies were assessed. The solar-to-fuel efficiency is defined as the ratio of the caloric value of the fuel produced to the solar power input absorbed by the reactor [39].

$$\eta_{solar\text{-}to\text{-}fuel} = F_{fuel}.\Delta H_{fuel}/P_{solar} \quad (8)$$

ΔH_{fuel} is the high heating value of produced fuel (286 $kJ.mol^{-1}$ for H_2, 283 $kJ.mol^{-1}$ for CO), F_{fuel} is the fuel production rate, and P_{solar} is the solar power input during the reduction step of the thermochemical cycle.

In addition, the cycle energy efficiency is defined as the ratio of the caloric value of the fuel produced to the energy required to heat ceria ($Q_{heating}$) and drive the endothermic reaction ($Q_{reaction}$) depending on the mole amount of processed ceria (n_{ceria}).

$$\eta_{cycle} = \int F_{fuel}dt.\Delta H_{fuel}/(Q_{heating}+Q_{reaction}) \quad (9)$$

with $Q_{heating} = n_{ceria}.\int c_{p.}dT$

and $Q_{reaction} = n_{ceria}.\Delta H_{CeO2\rightarrow CeO2-\delta}$

The ceria foams were fabricated following a standard replication method using polymer template commonly used for preparing commercial-grade porous catalysts and were supplied by ALSYS-CTI partner. The goal was to use standard commercial-grade foams usually developed for catalytic applications, in order to demonstrate their efficiency in solar redox cycles for both H_2O and CO_2 splitting without any further microstructure optimization. Future utilization of such foams in industrial-scale process should then be facilitated. The obtained foams after calcination of the polymer scaffold were fired at 1450°C during 10h under air to sinter and stabilize their structure. After sintering, the open-cell foams were composed of fine agglomerated ceria grains with interconnected macroporous channels around the grains facilitating the passage of the reacting gas. This type of microstructure was particularly attractive for the targeted solar redox cycle application. Indeed, the large mm-scale cells were suitable for volumetric solar radiation absorption during the reduction reaction, while the µm-

scale pores inside the foam struts favored the access of the reacting gas to the ceria bulk for the solid/gas oxidation reaction.

The cylindrical foams (45 mm diameter with 20 mm inner cavity diameter, 45 mm length) were inserted at the center of the cavity so that the upper side was just below the auxiliary gas inlet. The foams were composed of a bottom disc and 4 piled rings to form a centrally-hollowed cylinder with a closed bottom. With this arrangement, solar radiation can be more effectively captured along the foam height with the aim of achieving uniform heating of the whole reacting volume.

Foams with either uniform cell density (ppi, pores per inch) or cell density gradient in the axial direction (graded porosity) were used to evaluate the effect of pore size on temperature distribution and fuel production. Three different configurations were considered (Figure 1): (i) 4 different rings of 10, 20, 30, 45 ppi and a disc of 60 ppi, (ii) 2 rings of 10 ppi, 2 rings of 20 ppi and a disc of 60 ppi, (iii) 4 rings of 20 ppi and a disc of 10 ppi. In the following, these structures are designated as ceria foam with high cell density gradient (CF-HG), medium gradient (CF-MG) and no gradient (CF-NG), respectively. It is expected that increasing the cell density toward the bottom (lower cell size) enhances the optical thickness and reduces the radiation diffusion, thus increasing temperature gradient from the top to the bottom of the foam. Decreasing the cell size (higher ppi) also enhances the foam density, which increases the mass of reacting material loaded in the reactor. The total load of ceria foam was about 65 g (mean apparent density of ~1.1 g/cm^3).

3. Results and discussion

3.1. Cycling tests

The experimental study was conducted to demonstrate the solar reactor reliability during continuous on-sun operation and to determine the thermochemical performance metrics as a function of the operating conditions including the temperatures (during reduction and oxidation), pressure during reduction, cell density of the foam, oxidant flow rate and inlet mole fraction in the gas feed. The reactor performance was appraised based on the fuel yield, production rates evolution and energy conversion efficiency as the main evaluation criteria.

Prior to fuel production tests, blank experiments without any reactive material (empty cavity) were performed to confirm that the gas species production only evolves from the reactions

with ceria foam. As a result, no O_2 and H_2/CO were produced when heating the empty reactor in Ar up to 1400°C and subsequently feeding with H_2O or CO_2 when decreasing the temperature, which confirms the absence of side reactions with the reactor materials.

The different foams (CF-HG, CF-MG and CF-NG) underwent a total of 14, 18, and 32 cycles corresponding to 28h, 34h and 55h of continuous on-sun operation, respectively, with remarkable performance stability during cycling. In total, 2.6 L of H_2 (14 cycles) and 10.3 L (50 cycles) of CO were produced with an average per cycle of 2.8 mL/g and 3.4 mL/g for H_2 and CO, respectively (all volumes given at normal conditions, 0°C and 1 atm). The operating conditions along with the O_2 and CO/H_2 productions are listed in Table 1 for all the performed cycles. The average non-stoichiometry extent of the ceria foam (δ) and the fuel production yield in the course of the cycles performed with CF-NG are represented in Figure 2. Decreasing the pressure or increasing the temperature during reduction step strongly enhanced the non-stoichiometry extent reached by ceria as well as the fuel production yield. At nominal conditions (T_{red}=1400°C and T_{ox} below 1000°C), the fuel yield was ~200 µmol/g, without any performance decline thus confirming good thermal stability of the reactive foam. Unprecedented fuel production rates were achieved by carefully tuning the operating conditions and procedures during temperature-swing cycling. Among the investigated parameters, the oxidation temperature, the inlet CO_2 mole fraction and the CO:CO_2 ratio (calculated as $F_{CO,outlet}/F_{CO2,outlet}$) showed the most significant effect. The obtained fuel production rates outperformed the currently maximum reported values by up to 8 times using the manufactured ceria foams cycled between 1400°C and 900°C with oxidation performed upon dynamic cooling under 100% CO_2.

Table 1: Thermochemical cycles performed with CF-HG, CF-MG and CF-NG (Q_{Ar}=1.2 L:min during reduction, T_{red} and T_{ox} represent the reduction and oxidation temperatures given by T1 respectively, P_{red} the pressure during reduction, x the molar fraction of the oxidant gas, $Q_{tot,ox}$ the total inlet gas flow rate during oxidation step, volumes are given at normal conditions).

Cycle #	T_{red} (°C)	P_{red} (bar)	O_2 (µmol/g)	T_{ox} (°C)	x (oxidant)	$Q_{tot,ox}$ (L/min)	CO or H_2 (µmol/g)	Fuel production rate (mL/g/min)
CF-HG (m= 65.23 g)								
1	1342	0.883	85	1023	25% (CO_2)	1.6	154	1.0
2	1332	0.880	80	1089-801	25% (CO_2)	1.6	161	1.7
3	1277	0.880	57	1067-796	25% (CO_2)	1.6	113	1.5
4	1262	0.876	45	1040-786	50% (CO_2)	2.0	94	3.0
5	1331	0.858	77	974	25% (CO_2)	1.6	135	1.0
6	1327	0.874	74	828	25% (CO_2)	1.6	135	2.3
7	1323	0.873	69	836	50% (CO_2)	2.0	144	4.7
8	1332	0.867	82	831	100% (CO_2)	2.0	169	6.3
9	1363	0.871	93	1072-805	25% (CO_2)	1.6	184	1.7
10	1365	0.109	158	1065-670	25% (CO_2)	1.6	308	2.4
11	1364	0.105	152	1039-780	100% (CO_2)	2.0	341	6.6
12	1367	0.875	85	1176-669	17% (H_2O)	1.4	165	1.8
13	1363	0.905	95	1071-706	17% (H_2O)	1.4	169	6.5
14	1358	0.906	81	1183-644	17% (H_2O)	1.4	163	4.3
CF-MG (m= 65.30 g)								
1	1364	0.868	67	1053-800	25% (CO_2)	1.6	21	1.5
2	1362	0.871	89	694-623	25% (CO_2)	1.6	185	4.6
3	1409	0.871	131	1052-803	25% (CO_2)	1.6	259	1.7
4	1367	0.863	88	991	25% (CO_2)	1.6	171	1.0
5	1372	0.865	87	983	25% (CO_2)	1.6	167	0.9
6	1373	0.865	94	858	25% (CO_2)	1.6	195	2.3
7	1376	0.866	94	1064-819	25% (CO_2)	1.6	183	1.2
8	1374	0.107	152	1062-756	25% (CO_2)	1.6	300	2.1
9	1370	0.105	159	975-693	25% (CO_2)	1.6	267	2.2
10	1370	0.873	89	1007-691	17% (H_2O)	1.4	181	0.7
11	1377	0.909	92	1060-640	17% (H_2O)	1.4	201	0.6
12	1366	0.872	88	1049-686	20% (CO_2)	1.5	207	1.0
13	1370	0.860	92	999-790	17% (H_2O)	1.4	180	1.1
14	1369	0.875	87	1037-614	17% (H_2O)	1.4	185	1.0
15	1364	0.869	88	997-783	11% (H_2O)	2.2	199	0.8
16	1365	0.909	86	980-690	17% (H_2O)	1.4	187	1.2
17	1423	0.108	183	1056-831	100% (CO_2)	2.0	390	8.6
18	1371	0.876	100	1045-825	25% (CO_2)	1.6	184	1.2
CF-NG (m= 52.36 g)								
1	1379	0.871	81	1015-811	25% (CO_2)	1.6	182	2.6
2	1377	0.872	90	994-795	25% (CO_2)	1.6	190	3.2
3	1432	0.871	137	1018-826	25% (CO_2)	1.6	272	4.1
4	1381	0.871	89	876	25% (CO_2)	1.6	181	4.7

5	1380	0.113	138	1041-862	25% (CO_2)	1.6	238	3.2
6	1374	0.869	81	1088-634	17% (H_2O)	1.4	150	1.7
7	1378	0.867	79	1122-811	25% (CO_2)	1.6	200	2.1
8	1379	0.870	92	883	25% (CO_2)	1.6	205	3.3
9	1390	0.192	144	1053-816	25% (CO_2)	1.6	304	2.7
10	1437	0.872	119	1070-855	25% (CO_2)	1.6	241	2.1
11	1375	0.864	83	1026-883	25% (CO_2)	1.6	173	1.8
12	1375	0.867	89	1007-835	50% (CO_2)	2.0	194	4.2
13	1376	0.869	84	1038-875	100% (CO_2)	2.0	193	5.0
14	1374	0.872	133	982-796	25% (CO_2)	1.6	226	3.0
15	1377	0.874	86	1011-748	25% (CO_2)	0.8	170	1.2
16	1374	0.108	123	1006-811	25% (CO_2)	1.6	219	2.3
17	1385	0.856	91	1026-766	17% (H_2O)	1.5	179	0.7
18	1385	0.893	90	1054-697	40% (H_2O)	1.1	174	0.9
19	1050	0.893	10	911-796	17% (H_2O)	1.5	7	0.1
20	1376	0.857	86	1051-744	25% (CO_2)	1.6	186	1.5
21	1377	0.109	142	1044-815	100% (CO_2)	2.0	300	6.6
22	1380	0.116	132	1055-669	25% (H_2O)	1.7	235	1.1
23	1410	0.863	111	1052-823	100% (CO_2)	2.0	252	5.4
24	1408	0.864	104	1052-864	67% (CO_2)	3.0	225	4.7
25	1411	0.862	124	1054-839	50% (CO_2)	4.0	231	4.6
26	1350	0.863	65	1058-806	50% (CO_2)	4.0	134	2.9
27	1408	0.863	111	1044-895	50% (CO_2)	2.0	214	3.4
28	1408	0.863	104	1064-891	67% (CO_2)	3.0	207	4.7
29	1413	0.109	154	1049-867	67% (CO_2)	3.0	341	7.5
30	1407	0.868	101	1040-849	75% (CO_2)	4.0	242	6.6
31	1400	0.871	91	1052-886	50% (CO_2)	2.0	191	3.2
32	1402	0.110	146	899-753	100% (CO_2)	2.0	316	9.3

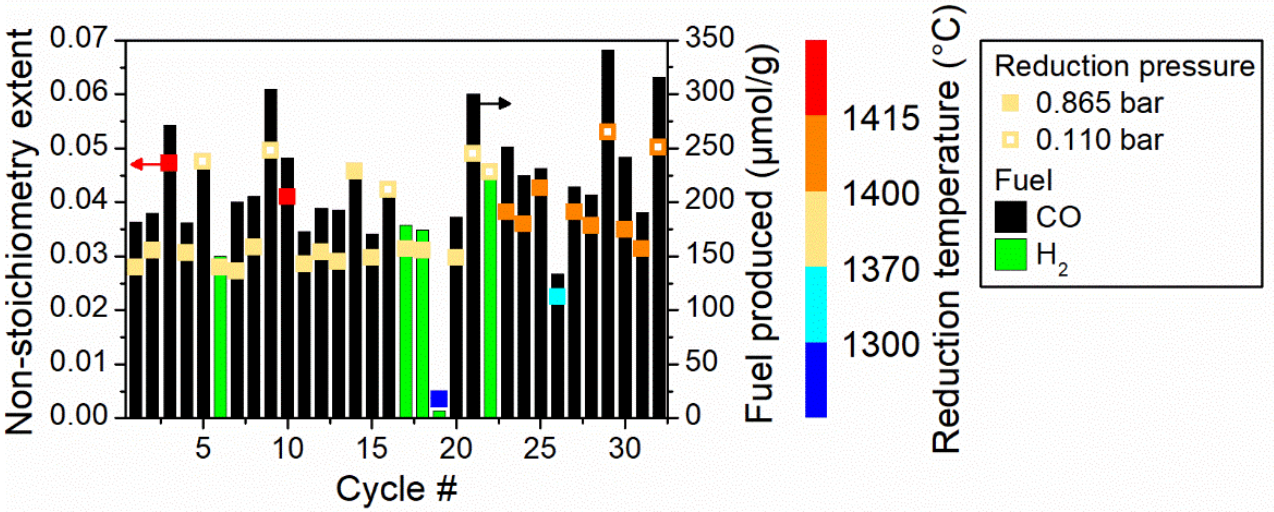

Figure 2: Non-stoichiometry extent δ (symbol) and fuel production yield (bar) during cycling (CF-NG). The symbol color indicates the reduction temperature, hollow symbols designate a reduction step performed at low pressure and the bar color represents the fuel type (H_2 or CO).

3.2. Pressure and temperature influence during reduction step

The temperature and the total pressure (affecting the oxygen partial pressure) are the two main parameters influencing the reduction extent reached by ceria. The influence of the reduction temperature on the reactor performance was investigated (Figure 3). The different temperature measurements along the foam height (T1-T3) revealed a temperature gradient within the reactive foam (axial direction), thus inducing a gradient in the reduction extent of the foam. The released oxygen increased from 57 to 93 µmol/g with the increase of the reduction temperature from 1280 to 1360°C (given by T1). For the highest reduction temperature, a maximal average ceria non-stoichiometry of δ=0.032 was achieved. During the oxidation step, the fuel production yield was enhanced from 113 µmol/g to 184 µmol/g, although the fuel production rate was not significantly impacted (slight increase from 1.5 to 1.7 mL/g/min). For a reduction temperature of 1360°C, the CO_2 conversion extent reached 5.3% and the CO_2 peak conversion rate reached 27.1% (in comparison with 3.5% and 24.8% for a reduction temperature of 1280°C). Increasing the reduction temperature thus improved the fuel production performance but the cycle temperature magnitude is limited by the material resistance to high temperatures (to avoid sintering or sublimation). Furthermore, a large temperature swing between reduction and oxidation steps induces heat losses and extension of cycling duration due to cooling/heating stages, then penalizing the global fuel productivity.

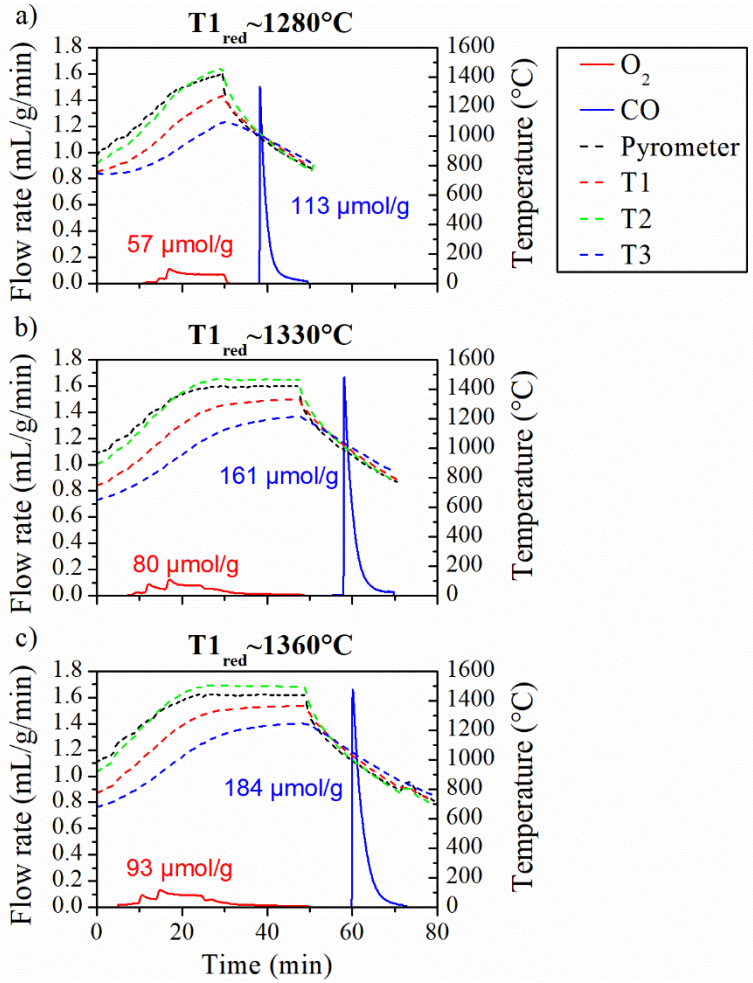

Figure 3: Evolution of O_2 and CO production rates with reduction temperature of a) 1280°C (cycle #3), b) 1330°C (cycle #2) and c) 1360°C (cycle #9) for CF-HG.

The other major operating parameter controlling the ceria reduction extent is the oxygen partial pressure.The effect of total pressure was investigated thanks to vacuum pumping by about one order of magnitude compared to atmospheric pressure (minimum achieved pressure of ~0.110 bar with flowing gas). Figure 4 compares two thermochemical cycles performed at atmospheric and low pressure during the reduction step. The O_2 yield increased from 86 µmol/g to 123 µmol/g with the pressure decrease from 0.875 bar to 0.108 bar. The non-stoichiometry extent reached δ=0.042 at 0.108 bar. During the oxidation step, the CO production yield was also enhanced (by 17%). Furthermore, the CO production rate rose from 1.5 to 2.3 mL/g/min. The CO_2 conversion extent was increased 2-fold (from 3.3% to 6.4%) with decreasing pressure, while the CO_2 peak conversion rate increased from 19.5% to 30.1%. A low pressure during the reduction step thus allowed reaching a high ceria non-stoichiometry, and showed a beneficial impact on both reduction and oxidation steps. The

theroretical minimum required power for pumping is given by: $P_{pump} = \dot{n}_{Ar} RT \ln\left(\frac{p_{atm}}{p_{reactor}}\right)$, where $\dot{n}_{Ar}$ is the Ar flow rate, $p_{reactor}$ and p_{atm} are the reactor and atmospheric pressures respectively. With Ar flow rate of 1.2 L/min and a reduced reactor pressure of 0.110 bar, the power consumption to decrease the reactor pressure is low (4 W) and negligible compared with the solar power input (1.5 kW) in the reactor. Therefore, the use of vacuum during the reduction step is attractive as it strongly enhances the ceria reduction extent while the energy penalties are restrained. However, the pressure swing while alternating reduction and oxidation steps may be a barrier for continuous process operation, and the pressure decrease magnitude should be kept easily accessible for being acceptable in large-scale processes.

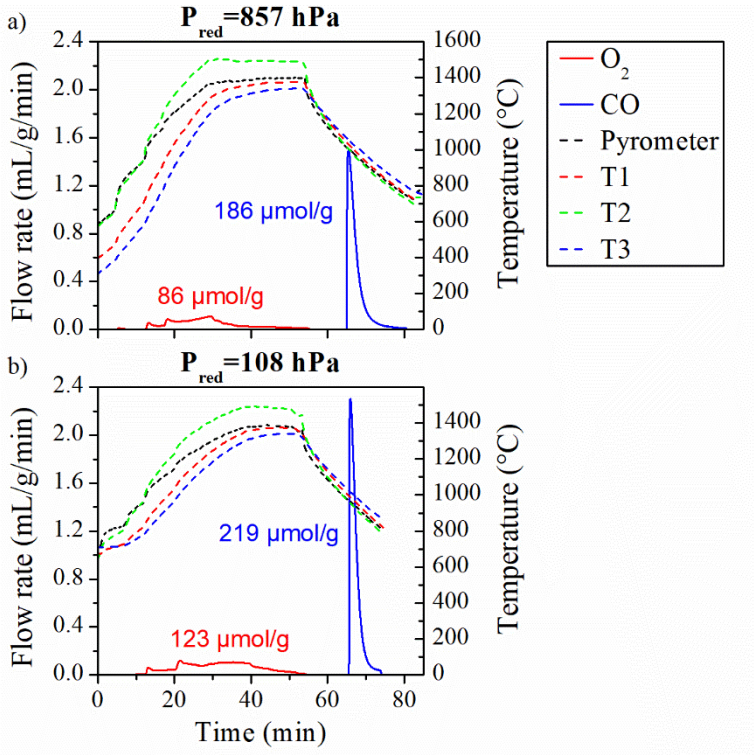

Figure 4: Thermochemical cycles performed with a) atmospheric (cycle #20) and b) reduced pressure (cycle #16) during the reduction step for CF-NG.

3.3. Oxidizing gas concentration and gas flow rates influence

Among the influencing parameters during the oxidation step, the inlet gas flow-rates play a major role and their impact on the fuel production has never been investigated. First the effect of total inlet flow rate (sum of inert and oxidant gas) was analyzed with a constant inlet molar fraction of the oxidant gas (CO_2). Figure 5 plots the CO production rates and CO:CO_2 mole

ratio for two different total flow rates with an inlet CO_2 molar fraction of 0.5. Doubling the total gas flow rate led to an increase of the CO peak production rate from 3.2 to 4.6 mL/g/min while the CO:CO_2 ratio decreased (from 0.21 to 0.14 for the maximum). Low CO:CO_2 ratio (and CO dilution) thus favored the oxidation rate. However, the lower the total gas flow rate, the higher the CO_2 conversion extent and CO_2 conversion peak (3.62% and 18% for 2 L/min compared with 1.53% and 12% for 4 L/min, respectively). In both cases, the ceria foam exhibited a re-oxidation extent superior to 90%. Therefore, a high total gas flow rate enhanced the production rate despite a negative impact on the CO_2 conversion.

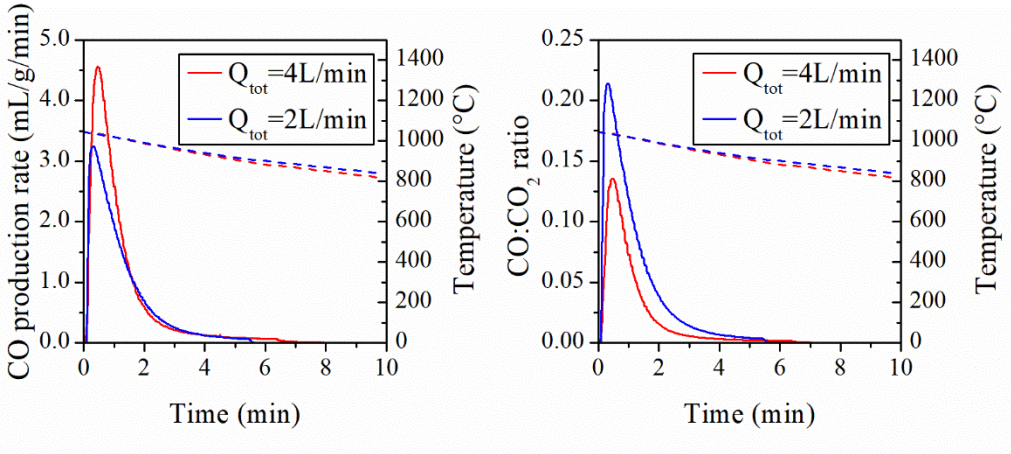

Figure 5: a) CO production rate (solid lines) and b) CO:CO_2 ratio (solid lines) along with T1 temperature (dashed lines) for total gas flow rates of 2 L/min (cycle #31) and 4 L/min (cycle #25) with CO_2 molar fraction of 0.5 for CF-NG.

Another important parameter during the oxidation step is the inlet molar fraction of the oxidant gas. Figure 6 presents the CO production rate and the CO:CO_2 mole ratio with two different inlet CO_2 molar fractions during the oxidation step (total inlet gas flow rate fixed at 2 L/min). Increasing the CO_2 molar fraction from 0.50 to 1.00 enhanced the CO production rate, with peak rates rising from 3.2 to 5.4 mL/g/min. This can be again explained by the lower CO:CO_2 ratio that favors the oxidation thermodynamic driving force, via a displacement of the reaction equilibrium due to the excess of one reagent (larger concentration of CO_2 favors the thermodynamic equilibrium towards CO production). However, increasing the CO_2 molar fraction hinders the CO_2 conversion extent that is decreased two-fold when doubling the CO_2 flow rate (cycle #23). Regardless of the CO_2 molar fraction, the ceria foam showed complete re-oxidation. In summary, a higher CO_2 molar fraction enhanced the CO production rate at the expense of a lower CO_2 conversion extent, which implies larger downstream separation work.

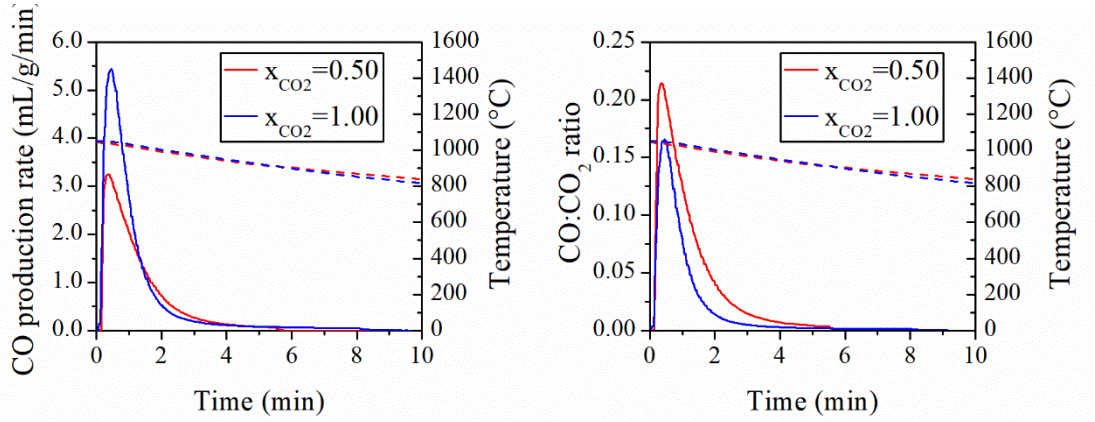

Figure 6: a) CO production rate (solid lines) and b) CO:CO_2 ratio (solid lines) along with T1 temperature (dashed lines) for CO_2 molar fraction of 0.50 (cycle #31) and 1.00 (cycle #23) with total gas flow rate fixed at 2 L/min (CF-NG).

During the oxidation step, the oxidizing gas can be diluted in inert gas. In order to study the impact of the Ar flow rate and dilution on the CO production rate, different Ar flow rates were used (0, 1, and 2 L/min) with fixed CO_2 flow rate (at 2 L/min), as represented in Figure 7. The peak CO production rate of 5.4 mL/min/g was achieved without any dilution whereas CO_2 dilution with Ar lowered the CO production rate. The CO production yield (in the range of 225-252 µmol/g) was not significantly impacted by the Ar dilution. Furthermore, the decrease of the CO_2 molar fraction arising from Ar dilution had an adverse impact and increasing the Ar flow did not show any beneficial effect on the oxidation step.

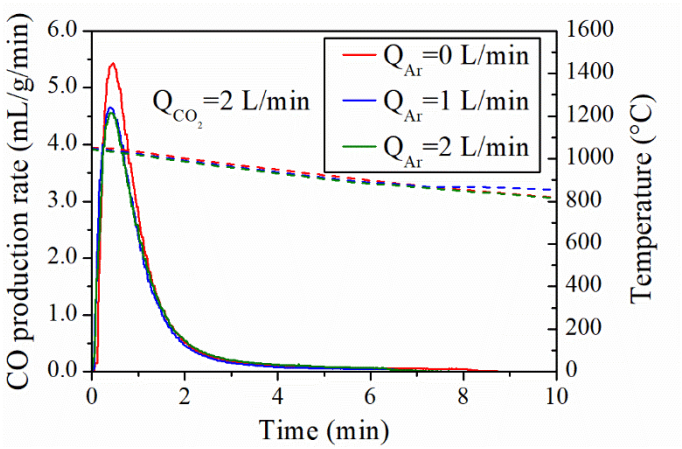

Figure 7: CO production rate (solid lines) along with T1 temperature (dashed lines) for different Ar flow rates (cycle #23 to #25 of CF-NG) at fixed CO_2 flow rate (2 L/min).

Finally, the inlet CO_2 flow rate represents a key parameter during the oxidation step. In order to investigate its effect on the CO production rate, cycles were performed with different CO_2 flow rates (from 1 L/min to 3 L/min) with Ar flow rate fixed at 1 L/min, as represented in Figure 8. It was demonstrated that the oxidation rate increases with inlet CO_2 concentration

(at constant total flow rate). Increasing inlet CO_2 flow rate also favors gas products dilution while inducing a drop in $CO:CO_2$ ratio, both favoring the oxidation reaction toward CO production. The higher the CO_2 flow rate, the higher the CO peak production rate (2-fold increase for CO_2 flow rate from 1 L/min to 3 L/min). The peak $CO:CO_2$ ratio reached 0.21 with CO_2 gas flow rate of 1 L/min (versus ~0.14 for cycles #30 and #24). The peak $CO:CO_2$ ratios are similar between 2 and 3 L/min of CO_2 gas flow because the higher amount of CO_2 is counterbalanced by the faster CO production rate. However, the CO_2 conversion extent is low when increasing the CO_2 flow rate (~1% with 3 L/min), which is not favorable on the process viewpoint since additional energy would be required to separate CO from unconverted CO_2. Therefore, tuning the CO_2 flow rate represents a trade-off to reach both maximum CO production rate and acceptable CO_2 conversion extent.

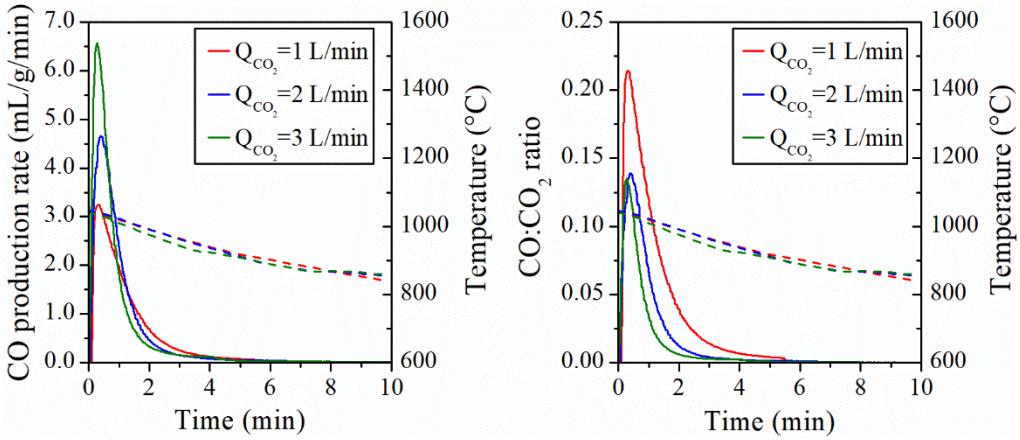

Figure 8: a) CO production rate (solid lines) and b) $CO:CO_2$ ratio (solid lines) along with T1 temperature (dashed lines) for CO_2 gas flow rate of 1 L/min (cycle #31), 2 L/min (cycle #24) and 3 L/min (cycle #30) at fixed Ar flow rate of 1 L/min (CF-NG).

As evidenced previously, a high CO_2 molar fraction during the oxidation step promotes a high CO production rate. The influence of the oxidizing gas was then investigated by carrying out the oxidation step with different water molar fractions (Figure 9). The H_2 production rate was only slightly increased when increasing over 2-fold the water molar fraction. The H_2 yield (in the range of 173-179 µmol/g) was not affected by the water concentration. Moreover, the cycle performed with x_{H2O}=0.17 showed both higher H_2O conversion extent and peak conversion (5.6% and 15.5%, respectively) in comparison with the cycle performed with x_{H2O}= 0.40 (2.6% and 10.2%, respectively). Unlike CO_2, steam molar fraction did not impact significantly the fuel production rate and increasing the H_2O concentration did not show strong benefit for improving the thermochemical performance. Since high H_2O conversion is targeted and steam production consumes energy, a low H_2O concentration is thus preferable.

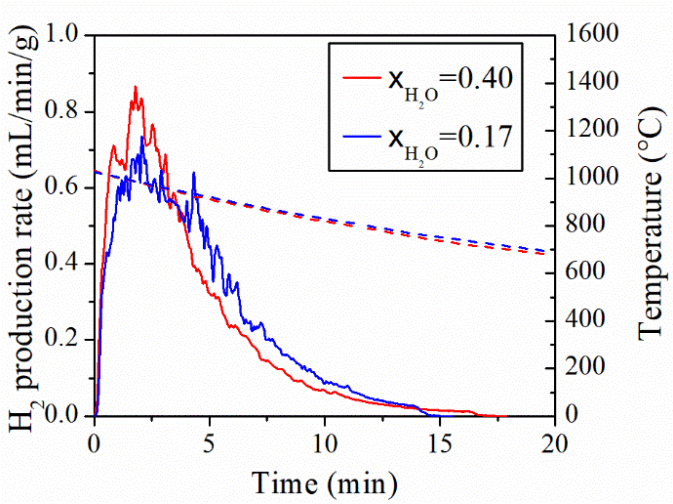

Figure 9: Influence of the steam water concentration on the H_2 production rate along with T1 temperature for CF-NG (cycles #17 and #18).

The fuel production profile shows a sharp peak as soon as the oxidant (H_2O or CO_2) is injected. The oxidation rate depends on the rate at which the oxidant is injected and reaches the reactive material, especially during the initial transient period of the oxidation while oxidant gas concentration rises. Hence, initial oxidation rate may be controlled by reactant feeding rate. The oxidant flow rate is fixed during the oxidation step but the targeted concentration is not reached instantaneously. Indeed, the oxidant concentration in the reactor increases during the initial period after oxidant gas injection until reaching the set point value. The increase of initial concentration is due to the replacement of the inert gas atmosphere by the injected oxidant, which is not immediate and depends on the inlet flow rate (that determines the time needed to fill the reactor cavity with oxidant gas). Besides, part of the injected oxidant is consumed by the reaction with ceria, which slows down the rise in oxidant concentration, especially at the start of the reaction. Thus, the initial oxidation rate increase can also be related to the transient increase of initial oxidant concentration after inlet gas switch.

3.4. Influence of foam cell size gradient

Foams with different cell size gradients forming a vertical graded porosity were considered to assess the thermochemical reactor performance according to the volumetric radiation absorption and resulting temperature distribution. Foams with larger cell sizes at top promote

volumetric solar absorption while small cell sizes promote the foam density (amount of loaded ceria). Figure 10 shows thermochemical cycles performed with the three foams exhibiting different porosity gradients. Increasing the cell size gradient led to higher temperature gradient within the ceria foam with temperature gaps from 150°C to 245°C (from the top to the bottom measured between T2 and T3). Increasing the cell density toward the bottom (CF-HG and CF-MG) enhanced the radiation attenuation, thus increasing the temperature gradient from the top to the bottom of the foam. In contrast, the foam with uniform cell density (20 ppi, CF-NG) led to the most uniform temperature distribution (as pointed out by the pyrometer temperature being similar to T1 and T3), thereby favoring more homogeneous reduction within the whole reacting structure. The overall O_2 and CO production yields (86-94 µmol/g and 184-186 µmol/g, respectively) were not influenced by the cell size gradient. This means that the temperature gradient did not modify the average oxygen non-stoichiometry and associated fuel production capacity of the graded foam structure.

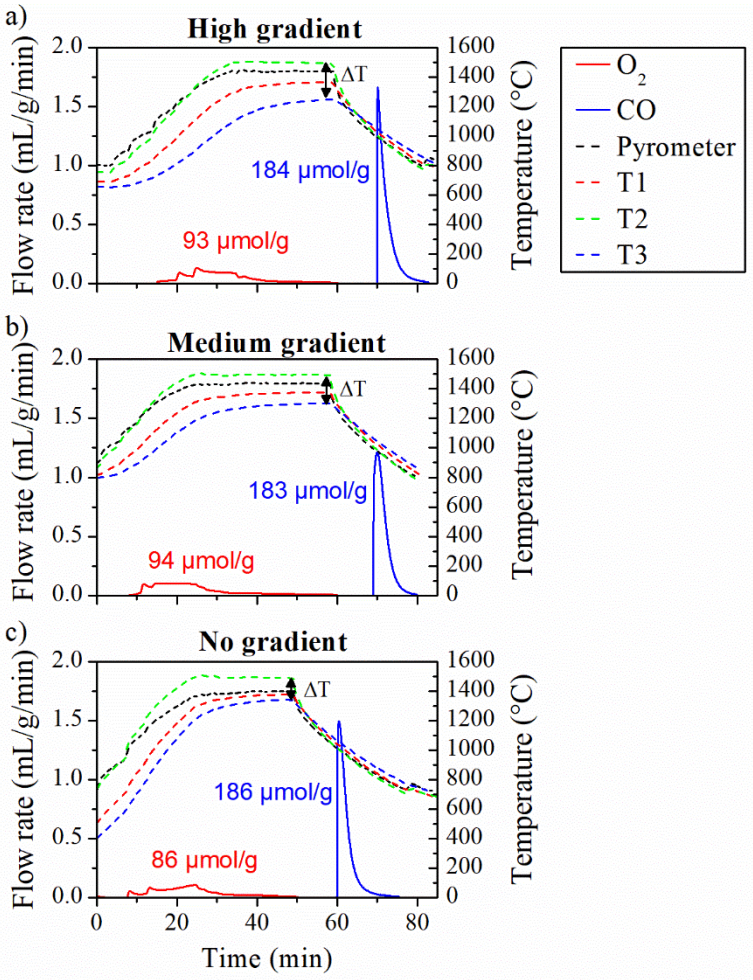

Figure 10: Thermochemical cycles performed at atmospheric pressure and T_{red}=1370°C with a non-isothermal oxidation (~1000-800°C) for a) CF-HG (cycle #9), b) CF-MG (cycle #7) and c) CF-NG (cycle #20).

In order to optimize the reactor performance, a thermochemical cycle (cycle #32 of CF-NG) was performed with the most favorable operating parameters identified previously (Figure 11). The O_2 and CO yields reached 146 µmol/g and 316 µmol/g, respectively. The CO_2 conversion extent was 2.79% while the peak CO_2 conversion was 25%. The cycle energy efficiency was 3.17% (with reduction enthalpy $\Delta H_{CeO2 \rightarrow CeO2-\delta}$ = 453 kJ/mol for δ=0.05 [40, 41], $Q_{reaction}$=137.8 kJ, and $Q_{heating}$=9.7 kJ assuming temperature swing of 400°C between reduction and oxidation steps), and the peak solar-to-fuel efficiency reached 7.5% (with P_{solar}=1.35 kW considering 10% of incident radiation losses caused by radiation attenuation by the window and reactor shadowing). The peak CO production rate achieved the highest value of 9.3 mL/g/min, thus representing a 8-fold increase compared with previous results (the highest fuel production rate reported to date, 1.2 mL/g/min, was obtained under more favorable conditions, i.e. temperature of 1500°C and pressure of 10 mbar during reduction [35–37]). The fast re-oxidation rate can be explained by the favorable microstructure of the

reactive foam exhibiting micro-scale interconnected porosity within the foam struts, as evidenced in the next section.

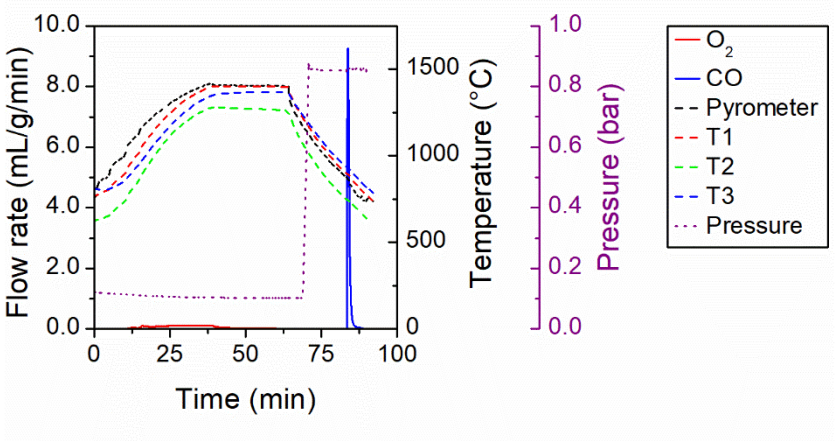

Figure 11: Maximum fuel production rate obtained with optimal conditions (cycle #32 of CF-NG at reduction temperature of 1400°C (T1), low pressure during reduction, oxidation starting at 900°C, CO_2 molar fraction of 1).

3.5. Morphological and microstructural characterization

The foam microstructure plays a key role in the thermochemical cycle performance, especially during the oxidation step which is a surface-controlled reaction. Scanning Electron Microscopy (SEM) was performed to unravel the foam microstructure and study the impact of the thermochemical cycles on the morphology. Figure 12 depicts the SEM images of the reactive foam before and after cycling (struts porosity, grain and pore size were estimated from ImageJ software). The foam struts of the unreacted foam are composed of micron-sized grains in the range of 3 to 10 µm forming interconnected micro-scale porosity (~13%, pore size from 1 to 5 µm), which is highly favorable for the access of gaseous reactant to the ceria grain surface during the oxidation step. In addition, numerous cracks on the surface are noticeable as well as cavities (hollow struts) resulting from the removal of the polymer template, which can also be beneficial for the oxidation step. After cycling, the ceria foam shows zones with different colors (white part situated at the top and grey part situated at the bottom of the foam). The white part of the foam presents slight densification (~10% porosity) compared with unreacted foam, presumably because of the high temperature occurring in the upper part of the foam (close to the zone receiving highly concentrated solar radiation). However, the grain growth remains limited (grain size below 12 µm and pores size up to 7 µm). The grey part is less densified with grain size in the range 3-12 µm (~12% porosity and

pores size up to 6 µm). The reactive foams thus exhibit a good thermal stability and resistance to sintering over cycles that is essential to extended solar process operation.

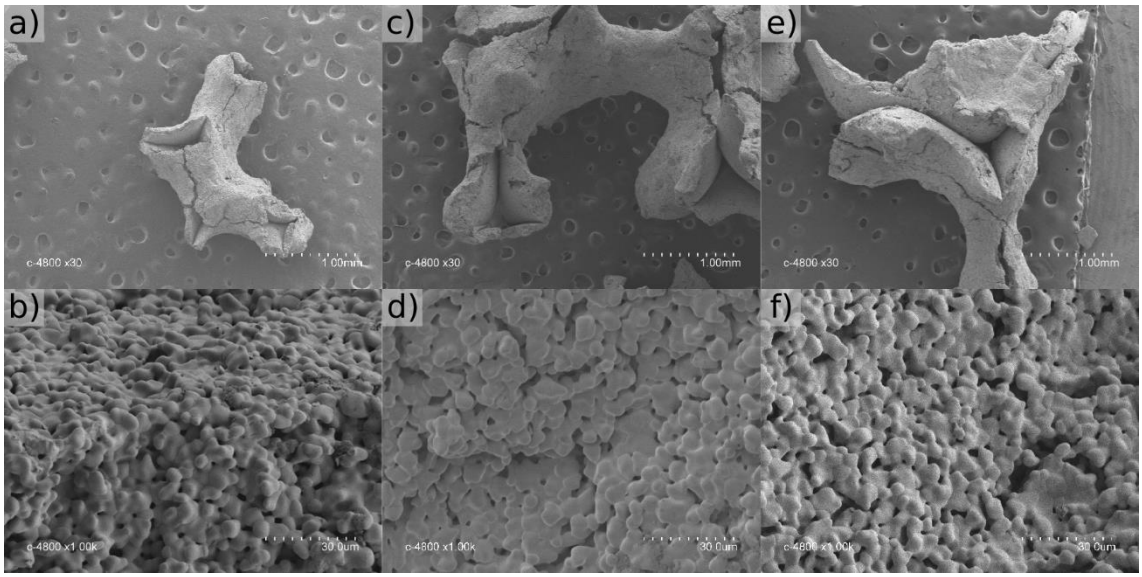

Figure 12: SEM micrographs for a) and b) unreacted foam (10 ppi ring), c) and d) white part (top of the foam) after cycling, e) and f) grey part (bottom of the foam) after cycling

4. Conclusion

A new solar chemical reactor integrating highly-reactive ceria open-cell foams was designed and operated for two-step thermochemical H_2O and CO_2 splitting. Remarkable fuel production rates and yields as well as material performance stability were achieved during continuous on-sun operation with the manufactured commercial-grade ceria foams exhibiting volumetric solar absorption via mm-scale open cells and relevant porous microstructure favoring solid-gas surface reactions. The foam structures with axial graded porosity showed magnified temperature gradient that did not alter the overall fuel production capacity. Hence, the cell size gradient in foams did not exhibit any significant impact on the fuel production yield. Stable CO and H_2 production was demonstrated in the monolithic solar reactor. The reduction extent was improved by increasing the reduction temperature or decreasing the pressure during reduction step. Increasing inlet oxidant molar concentration or total gas flow-rate enhanced the fuel production rate. A boost of the fuel production rate (by a factor of ~8) was obtained in the developed solar reactor heated by real concentrated solar radiation, thus outperforming the previous maximum values reported to date with less stringent conditions on the reduction temperature (~1400°C) and pressure (atmospheric down to ~0.1 bar), and by

carrying out the oxidation step in pure CO_2 upon free reactor cooling. Such noteworthy performance was achieved by optimized solar reactor configuration, relevant control of the ceria foam microstructure (micron-sized grains forming interconnected porosity in the foam struts), optimal design of the 3D reactive structures, thorough investigation of the cycle parameters influence and suitable tuning of the operating conditions. The entire fuel production chain was thus demonstrated, spanning from suitable redox material shaping (for their integration as volumetric solar absorber) to reactor design and solar operation. This represents a significant step-forward in demonstration of ceria redox cycle under real solar processing conditions and future reactor scale up.

Next work should focus on the geometric optimization of the 3D porous structures via thermal and fluid dynamics modelling for achieving uniform temperature distribution and reaction extent, as well as the shaping of porous reactive ceramics with controlled microstructure.

Acknowledgments

This work was funded by the French National Agency for Research (ANR, SUNFUEL project, contract N°ANR-16-CE06-0010). The authors thank R. Garcia (PROMES) for solar reactor design, V. Bollee and J. Valls (Alsys-CTI) for supplying the ceria foams.

References

[1] N. S. Lewis and D. G. Nocera, "Powering the planet: Chemical challenges in solar energy utilization," *Proc. Natl. Acad. Sci. U.S.A.*, vol. 103, no. 43, pp. 15729–15735, 2006.

[2] L. Barreto, A. Makihira, and K. Riahi, "The hydrogen economy in the 21st century: a sustainable development scenario," *Int. J. Hydrogen Energy*, vol. 28, no. 3, pp. 267–284, 2003.

[3] C. Green, S. Baksi, and M. Dilmaghani, "Challenges to a climate stabilizing energy future," *Energy Policy*, vol. 35, no. 1, pp. 616–626, 2007.

[4] C. Graves, S. D. Ebbesen, M. Mogensen, and K. S. Lackner, "Sustainable hydrocarbon fuels by recycling CO_2 and H_2O with renewable or nuclear energy," *Renew. Sustain. Energ. Rev.*, vol. 15, no. 1, pp. 1–23, 2011.

[5] G. Centi and S. Perathoner, "Opportunities and prospects in the chemical recycling of carbon dioxide to fuels," *Catal. Today*, vol. 148, no. 3–4, pp. 191–205, 2009.

[6] J. D. Holladay, J. Hu, D. L. King, and Y. Wang, "An overview of hydrogen production technologies," *Catal. Today*, vol. 139, no. 4, pp. 244–260, 2009.

[7] N. Muradov and T. Veziroglu, "'Green' path from fossil-based to hydrogen economy: An overview of carbon-neutral technologies," *Int. J. Hydrogen Energy*, vol. 33, no. 23, pp. 6804–6839, 2008.

[8] S. Abanades, P. Charvin, G. Flamant, and P. Neveu, "Screening of water-splitting thermochemical cycles potentially attractive for hydrogen production by concentrated solar energy," *Energy*, vol. 31, no. 14, pp. 2805–2822, 2006.

[9] H. Herzog and D. Golomb, "Carbon capture and storage from fossil fuel use," *Encyclopedia of Energy*, Elsevier, pp. 277–287, 2004.

[10] V. P. Indrakanti, J. D. Kubicki, and H. H. Schobert, "Photoinduced activation of CO_2 on Ti-based heterogeneous catalysts: Current state, chemical physics-based insights and outlook," *Energy Environ. Sci.*, vol. 2, no. 7, p. 745, 2009.

[11] J. R. Scheffe and A. Steinfeld, "Oxygen exchange materials for solar thermochemical splitting of H_2O and CO_2: a review," *Mater. Today*, vol. 17, no. 7, pp. 341–348, 2014.

[12] S. Abanades and M. Chambon, "CO_2 Dissociation and Upgrading from Two-Step Solar Thermochemical Processes Based on ZnO/Zn and SnO_2 /SnO Redox Pairs," *Energ. Fuel*, vol. 24, no. 12, pp. 6667–6674, 2010.

[13] T. Kodama, Y. Kondoh, R. Yamamoto, H. Andou, and N. Satou, "Thermochemical hydrogen production by a redox system of ZrO_2-supported Co(II)-ferrite," *Sol. Energy*, vol. 78, no. 5, pp. 623–631, 2005.

[14] J. E. Miller, M. D. Allendorf, R. B. Diver, L. R. Evans, N. P. Siegel, and J. N. Stuecker, "Metal oxide composites and structures for ultra-high temperature solar thermochemical cycles," *J. Mater. Sci.*, vol. 43, no. 14, pp. 4714–4728, 2008.

[15] R. Jacot, J. M. Naik, R. Moré, R. Michalsky, A. Steinfeld, and G. R. Patzke, "Reactive stability of promising scalable doped ceria materials for thermochemical two-step CO_2 dissociation," *J. Mater. Chem. A*, vol. 6, no. 14, pp. 5807–5816, 2018.

[16] W. C. Chueh and S. M. Haile, "A thermochemical study of ceria: exploiting an old material for new modes of energy conversion and CO_2 mitigation," *Phil. Trans. R. Soc. A*, vol. 368, no. 1923, pp. 3269–3294, 2010.

[17] B. Bulfin, A. J. Lowe, K. A. Keogh, B. E. Murphy, O. Lübben, S. A. Krasnikov, and I. V. Shvets, "Analytical Model of CeO_2 Oxidation and Reduction," *J. Phys. Chem. C*, vol. 117, no. 46, pp. 24129–24137, 2013.

[18] G. Takalkar, R. R. Bhosale, and F. AlMomani, "Thermochemical splitting of CO_2 using Co-precipitation synthesized $Ce_{0.75}Zr_{0.2}M_{0.05}O_{2-\delta}$ (M = Cr, Mn, Fe, CO, Ni, Zn) materials," *Fuel*, vol. 256, p. 115834, 2019.

[19] Y. Lu, L. Zhu, C. Agrafiotis, J. Vieten, M. Roeb, and C. Sattler, "Solar fuels production: Two-step thermochemical cycles with cerium-based oxides," *Progress in Energy and Combustion Science*, vol. 75, p. 100785, 2019.

[20] A. Haeussler, S. Abanades, J. Jouannaux, M. Drobek, A. Ayral, and A. Julbe, "Recent progress on ceria doping and shaping strategies for solar thermochemical water and CO_2 splitting cycles," *AIMS Mater. Sci.*, vol. 6, no. 5, pp. 657–684, 2019.

[21] A. Trovarelli, "Catalytic Properties of Ceria and CeO_2 -Containing Materials," *Catal. Rev.*, vol. 38, no. 4, pp. 439–520, 1996.

[22] R. Jacot, R. Moré, R. Michalsky, A. Steinfeld, and G. R. Patzke, "Trends in the phase stability and thermochemical oxygen exchange of ceria doped with potentially tetravalent metals," *J. Mater. Chem. A*, vol. 5, no. 37, pp. 19901–19913, 2017.

[23] C. Muhich and A. Steinfeld, "Principles of doping ceria for the solar thermochemical redox splitting of H_2O and CO_2," *J. Mater. Chem. A*, vol. 5, no. 30, pp. 15578–15590, 2017.

[24] A. Le Gal and S. Abanades, "Catalytic investigation of ceria-zirconia solid solutions for solar hydrogen production," *Int. J. Hydrogen Energy*, vol. 36, no. 8, pp. 4739–4748, 2011.

[25] F. Call, M. Roeb, M. Schmücker, C. Sattler, and R. Pitz-Paal, "Ceria Doped with Zirconium and Lanthanide Oxides to Enhance Solar Thermochemical Production of Fuels," *J. Phys. Chem. C*, vol. 119, no. 13, pp. 6929–6938, 2015.

[26] D. Arifin, A. Ambrosini, S. A. Wilson, B. Mandal, C. L. Muhich, and A. W. Weimer, "Investigation of Zr, Gd/Zr, and Pr/Zr – doped ceria for the redox splitting of water," *Int. J. Hydrogen Energy*, vol. 45, no. 1, pp. 160–174, 2020.

[27] R. R. Bhosale, A. Kumar, F. AlMomani, U. Ghosh, S. Al-Muhtaseb, R. Gupta, and I. Alxneit, "Assessment of $Ce_xZr_yHf_zO_2$ based oxides as potential solar thermochemical CO_2 splitting materials," *Ceram. Int.*, vol. 42, no. 8, pp. 9354–9362, 2016.

[28] G. Luciani, G. Landi, C. Imparato, G. Vitiello, F. A. Deorsola, A. Di Benedetto, and A. Aronne, "Improvement of splitting performance of $Ce_{0.75}Zr_{0.25}O_2$ material: Tuning bulk and surface properties by hydrothermal synthesis," *Int. J. Hydrogen Energy*, vol. 44, no. 33, pp. 17565–17577, 2019.

[29] Z. Zhao, M. Uddi, N. Tsvetkov, B. Yildiz, and A. F. Ghoniem, "Redox Kinetics and Nonstoichiometry of $Ce_{0.5}Zr_{0.5}O_{2-\delta}$ for Water Splitting and Hydrogen Production," *J. Phys. Chem. C*, vol. 121, no. 21, pp. 11055–11068, 2017.

[30] Y. Hao, C.-K. Yang, and S. M. Haile, "Ceria–Zirconia Solid Solutions ($Ce_{1-x}Zr_xO_{2-\delta}$, $x \leq 0.2$) for Solar Thermochemical Water Splitting: A Thermodynamic Study," *Chem. Mater.*, vol. 26, no. 20, pp. 6073–6082, 2014.

[31] S. Abanades and G. Flamant, "Thermochemical hydrogen production from a two-step solar-driven water-splitting cycle based on cerium oxides," *Sol. Energy*, vol. 80, no. 12, pp. 1611–1623, 2006.

[32] S. Abanades, A. Legal, A. Cordier, G. Peraudeau, G. Flamant, and A. Julbe, "Investigation of reactive cerium-based oxides for H_2 production by thermochemical two-step water-splitting," *J. Mater. Sci.*, vol. 45, no. 15, pp. 4163–4173, 2010.

[33] A. Demont and S. Abanades, "Solar thermochemical conversion of CO_2 into fuel via two-step redox cycling of non-stoichiometric Mn-containing perovskite oxides," *J. Mater. Chem. A*, vol. 3, no. 7, pp. 3536–3546, 2015.

[34] S. Abanades and A. Le Gal, "CO_2 splitting by thermo-chemical looping based on $Zr_xCe_{1-x}O_2$ oxygen carriers for synthetic fuel generation," *Fuel*, vol. 102, pp. 180–186, 2012.

[35] D. Marxer, P. Furler, M. Takacs, and A. Steinfeld, "Solar thermochemical splitting of CO_2 into separate streams of CO and O_2 with high selectivity, stability, conversion, and efficiency," *Energ. Environ. Sci.*, vol. 10, no. 5, pp. 1142–1149, 2017.

[36] P. Furler, D. Marxer, M. Takacs, and A. Steinfeld, "Solar thermochemical reactor technology for splitting CO_2," *AIP Conference Proceedings*, vol. 2033, no. 1, p. 130005, 2018.

[37] P. Furler, D. Marxer, J. Scheffe, D. Reinalda, H. Geerlings, C. Falter, V. Batteiger, A. Sizmann, and A. Steinfeld, "Solar kerosene from H_2O and CO_2," *AIP Conference Proceedings*, vol. 1850, no. 1, p. 100006, 2017.

[38] H. I. Villafán-Vidales, C. A. Arancibia-Bulnes, D. Riveros-Rosas, H. Romero-Paredes, and C. A. Estrada, "An overview of the solar thermochemical processes for hydrogen and syngas production: Reactors, and facilities," *Renew. Sustain. Energ. Rev.*, vol. 75, pp. 894–908, 2017.

[39] A. Haeussler, S. Abanades, A. Julbe, J. Jouannaux, M. Drobek, A. Ayral, and B. Cartoixa, "Remarkable performance of microstructured ceria foams for thermochemical splitting of H_2O and CO_2 in a novel high-temperature solar reactor," *Chem. Eng. Res. Des.*, vol. 156, pp. 311–323, 2020.

[40] R. J. Panlener, R. N. Blumenthal, and J. E. Garnier, "A thermodynamic study of nonstoichiometric cerium dioxide," *J. Phys. Chem. Solids*, vol. 36, no. 11, pp. 1213–1222, 1975.

[41] C.-K. Yang, Y. Yamazaki, A. Aydin, and S. M. Haile, "Thermodynamic and kinetic assessments of strontium-doped lanthanum manganite perovskites for two-step thermochemical water splitting," *J. Mater. Chem. A*, vol. 2, no. 33, pp. 13612–13623, 2014.